Ultra-Thin Broadband Circular Polarization Conversion Metasurface for Full-Space Wavefront Manipulation Application

Bingzhen Li, Yuhua Chen, Songlin Yu, Xiao Zhou, Qingqing Wu, Jijun Wang, Yan Li, and Fangyuan Li

***Abstract*—In this article, we introduced an ultra-thin broadband single-layer metasurface (MS) comprising an S-shaped resonator (SSR) structure enclosed by a circular cover adhered on a dielectric substrate. The MS exhibits remarkable capabilities in achieving simultaneous half-transmission and half-reflection for broadband circular polarization (CP) conversion, as well as full-space wavefront manipulation in the microwave frequency range. Through simulations and experiments, we demonstrated that the orthogonal CP coefficients for both transmission and reflection exceed 0.35 for normal incidence of left-handed circular polarizations (LCP) and right-handed circular polarizations (RCP) waves from 6.2 GHz to 15 GHz, with a relative bandwidth of about 87.1%. This results in a polarization conversion efficiency of approximately 22%, which approaches the theoretical limit (25%) of the single layer MS structure around 8 GHz. Moreover, utilizing the principle of geometrical phase modulation, the desired full 2π phase-shift of orthogonal CP waves in both transmission and reflection can be achieved by solely adjusting the orientation angle of the SSR structure. Numerical simulations substantiate this concept by demonstrating anomalous reflection and refraction, vortex beam generation, and planar focusing, showcasing the comprehensive control of wavefronts in all spatial directions. Our design offers valuable insights for the practical implementation of broadband full-space CP and wavefront manipulation in various applications.**

***Index Terms*—Circular polarization, polarization conversion, broadband, metasurface, wavefront manipulation.**

I. Introduction

OVER the past decade, metasurfaces (MSs), which are two-dimensional (2D) planar structures of metamaterials (MMs), have emerged as a prominent research frontier for scientific and engineering communities. This popularity stems from their facile fabrication and remarkable ability to manipulate electromagnetic (EM) waves, as observed by various researchers [1], [2]. Compared to bulk MMs, MSs offer notable advantages, such as reduced dimensionality and simplified fabrication processes, alongside unique features like lighter weight, lower loss, and thinner thickness. Consequently, MSs have provided an exceptionally versatile and promising platform for exploring a wide range of intriguing phenomena and developing novel devices. Notable examples include perfect absorption [3], [4], field enhancement effects [5], extraordinary transmission [6], polarization conversion [7], [8], holographic imaging [9], [10], anomalous scattering [11], focusing [12], [13], radar cross-section (RCS) reduction [14], high-gain antennas [15], [16], [17], vortex beam generators [18], [19], [20], and more. Polarization conversion and wavefront manipulation enabled by MSs play a pivotal role in a wide range of practical applications, including subwavelength resolution imaging, cloaking, and wireless communications [21], [22], [23]. Consequently, numerous MS-based designs have been proposed and investigated, driving the rapid advancement of polarization conversion and wavefront manipulation devices [24], [25], [26], [27], [28], [29], [30], [31], [32]. For instance, Yu et al. presented a dual-band double-arrow MS capable of manipulating the polarization states of EM waves [24], while Liu et al. introduced a single-layer reflective MS for generating high-order Bessel vortex beams [25]. Furthermore, Wang et al. proposed an all-metal MS that achieves highly efficient reflective circular-polarization (CP) conversion and wavefront manipulation in the terahertz (THz) region [28]. These studies exemplify the diverse range of MS designs aimed at expanding the capabilities of polarization conversion and wavefront manipulation for practical applications.

While many of the aforementioned MSs excel in manipulating either transmitted or reflected EM waves with diverse functionalities, these functionalities may not fully satisfy the demands of modern EM applications concerning miniaturization and multifunctional integration. In order to enhance the efficiency of space resource utilization, there is a growing need for full-space MSs that can manipulate both transmission and reflection simultaneously [33], [34], [35], [36]. As a result, there has been a notable surge in attention and considerable efforts dedicated to the simultaneous or independent manipulation of reflected and transmitted EM waves [37], [38], [39], [40], [41], [42], [43], [44], [45], [46]. As an example, Cai et al. introduced a novel type of MS capable of manipulating full-space EM waves by exhibiting polarization-dependent reflection and transmission properties [35]. In a similar vein, Muhammad et al. conducted experimental demonstrations of an exceptionally thin MS, consisting of a single metallic layer, capable of generating vortex waves carrying orbital angular momentum (OAM), as well as enabling anomalous reflections and refractions [37]. Furthermore, Li et al. proposed a comprehensive full-space MS that can independently manipulate transmitted linear polarization (LP) and reflected CP

Manuscript received 29 May 2023; revised 22 June 2023; accepted 26 June 2023. Date of publication 7 July 2023; date of current version 26 July 2023. *(Corresponding authors: Jijun Wang; Yan Li; Fangyuan Li.)*

The authors are with the Institute of Defense Engineering, Academy of Military Science of the PLA, Beijing 100036, China (e-mail: wangjjghs@163.com; 214360618@qq.com; 775245805@qq.com).

Digital Object Identifier 10.1109/JPHOT.2023.3290365

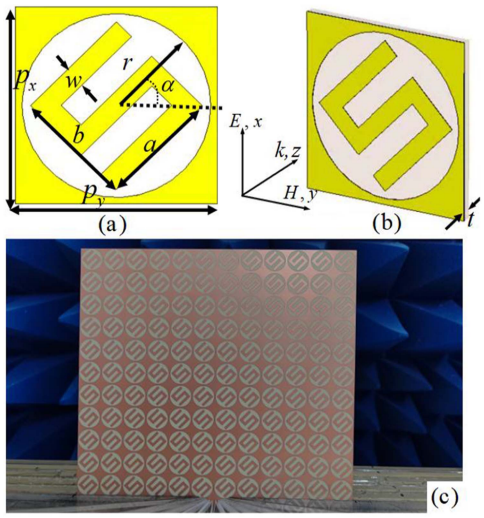

Fig. 1. Schematic diagram of the (a) front and (b) perspective view of the unit-cell and (c) the fabricated sample of the proposed MS.

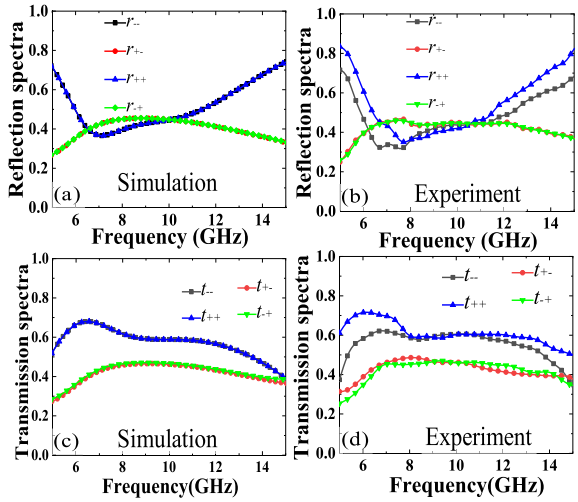

Fig. 2. (a), (c) simulated and (b), (d) measured (a), (b) reflection and (c), (d) transmission spectra of the designed single layer MS for the normal incident LCP and RCP wave propagation along the z-axis direction.

waves [46]. Nonetheless, despite these advancements, most multifunctional MSs still face challenges such as lower efficiency or narrowband operation, often due to limitations imposed by their single-layer or multi-layer structural designs.

In this study, we present an ultrathin, single-layer MS consisting of metal resonator structures capable of achieving broadband CP conversion and multifunctional wavefront manipulation for both reflection and transmission in the microwave region. Initially, we demonstrated the design of the MS structure and validate the broadband CP conversion for reflection and transmission through numerical simulations and experimental measurements. Furthermore, we illustrate that by rotating the orientation of the proposed MS unit-cell structure, a complete 2π phase-shift can be simultaneously achieved for both reflection and transmission, enabling comprehensive multifunctional wavefront manipulation across all spatial directions. To substantiate the concept, we provide proof-of-concept examples, including numerical simulations of anomalous refraction and reflection, vortex beam generation, and planar focusing effects. The proposed MS holds significant potential for enabling broadband and multifunctional manipulation of EM waves in various full-space applications.

II. Design, Simulation and Experiment

The proposed MS is depicted in Fig. 1, showcasing a periodic arrangement of copper S-shaped resonator (SSR) structures encased by copper circular covers affixed to an ultrathin dielectric substrate. The unit-cell structure of the single-layer MS is presented in Fig. 1(a) and (b), offering front and perspective views, respectively.

In line with previous MS designs [34], [38], [39], [40], the SSR structure functions as a dipole resonator, effectively interacting with the electric component of the incident EM wave and facilitating broad-spectrum polarization conversion. Additionally, Fig. 1(a) showcases the SSR structure with a localized orientation angle denoted as α relative to the y-axis direction. This characteristic served as an inspiration for utilizing the SSR structure, in conjunction with copper circular covers, as the resonator structure to achieve efficient CP conversion across a wide frequency range. The designed MS unit-cell exhibits optimized structural parameters, outlined as follows: $p_x = p_y = 15$ mm, $r = 7$ mm, $a = b = 9$ mm, $w = 1.6$ mm, $t = 0.8$ mm.

To evaluate the performance and efficiency of the designed single-layer MS, comprehensive full-wave simulations were conducted employing the finite integration technique (FIT) and the frequency domain solver available in the CST Microwave Studio. For the simulation, the metallic structure layer was modeled using copper with an electric conductivity of $\sigma = 5.8 \times 10^7$ S/m. As for the dielectric substrate, the microwave board Rogers RO4350 with a relative permittivity of $\varepsilon_r = 4.2(1 + 0.0037\text{i})$ was chosen. To validate the efficiency of the proposed MS experimentally, a test sample consisting of a 12×12 array of unit-cells was fabricated using the conventional printed circuit board (PCB) process. The dimensions of the sample were 180 mm $\times$ 180 mm $\times$ 0.8 mm. The two broadband planar spiral CP antennae connected to a vector network analyzer (Agilent E8362B) by coaxial cable were used to measure the reflection (r_{++}, r_{--}, r_{+-} and r_{-+}) and transmission (t_{++}, t_{--}, t_{+-} and t_{-+}) coefficients for the left-handed circular polarization (LCP) and right-hand circular polarization (RCP) waves from 3 to 17 GHz.

III. Results and Disscussions

A. Broadband CP Conversion With Half-Transmission and Half-Reflection

To commence our investigation, we assess the CP conversion performance of the proposed MS in the context of both reflection and transmission for normally incident left-handed circularly polarized (LCP) and right-handed circularly polarized (RCP) waves. Fig. 2 presents the reflection and transmission spectra

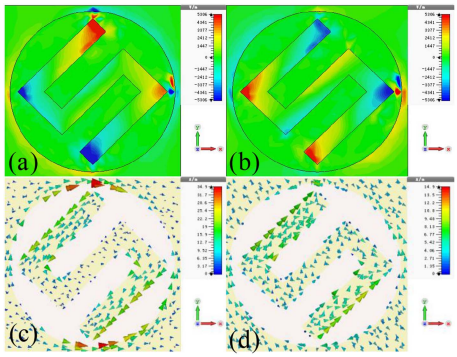

Fig. 3. Simulated (a), (b) electric field (z-component, E_z) and (c), (d) surface current distributions of the unit-cell structure at (a), (c) 7 GHz and (b), (d) 11GHz for the normal incident LCP wave.

of the single-layer MS, as observed in both simulations and experimental measurements, for LCP and RCP waves propagating along the z-axis direction. Remarkably, the measured amplitudes of the reflected and transmitted CP waves align closely with the simulation results, indicating a good agreement. There are some minor difference between simulation and experiment for the reflection and transmission under the incident LCP and RCP wave. Several possible factors could account for these differences, including: (1) minor discrepancies in the permittivity of the Rogers RO4350 board substrate and the metallic structure thickness during the fabrication process; (2) the influence of finite sizes of the metasurface slab, which were considered in the measurements but not accurately simulated or calculated in practical terms; and (3) potential imperfections and tolerances in the test environment.

Fig. 2(a) and (b) present the amplitude characteristics of the reflected orthogonal circularly polarized (CP) wave, as obtained through simulations and experimental measurements. Throughout the frequency range of 5–15 GHz, both the simulated and measured amplitudes consistently exceed 0.25, with a peak value of 0.47 observed at 8–10 GHz. Similarly, Fig. 2(c) and (d) exhibit corresponding amplitude curves for the transmitted orthogonal CP wave, which also maintain amplitudes above 0.25 across the broad frequency range of interest. Remarkably, the designed MS possesses an ultra-thin profile, with a thickness of merely 0.8 mm, representing approximately 1/37.5 of the operating wavelength at 10 GHz. Notably, the amplitudes of the reflected and transmitted orthogonal CP waves remain nearly identical throughout the entire frequency range. These findings demonstrate that the proposed MS can effectively convert a portion of the incident LCP or RCP wave into its orthogonal CP component, achieving simultaneous reflection and transmission across the broadband spectrum. Additionally, the CP conversion efficiency for both reflection and transmission modes averages approximately 22% across the entire frequency range, with a near-uniform efficiency of around 25% near 8 GHz, approaching the theoretical limit for an infinitesimally thin MS.

To elucidate the underlying physical mechanism responsible for the CP conversion in our design, Fig. 3 showcases the spatial distribution of the instantaneous induced electric field (E_z) and surface currents within the unit-cell structure, excited by incident LCP waves at two distinct resonance frequencies, namely 7 GHz and 11 GHz.

The plots in Fig. 3(a) and (b) reveal an enhanced E_z field within the unit-cell, indicating a significant accumulation of charge along the edges of the SSR structure and circular cover structures at these respective frequencies. This observation suggests that the CP conversion phenomenon in our design primarily originates from a simple electric dipole-dipole interaction. Furthermore, the induced surface currents depicted in Fig. 3(c) and (d) exhibit similar characteristics in both frequency bands, albeit with reversed flow directions. This intriguing behavior implies that the CP conversion performance can be effectively maintained across a wide frequency range. Consequently, our proposed single-layer MS serves as a versatile wideband CP converter, simultaneously achieving half-reflection and half-transmission capabilities.

B. Multi-Functional Full-Space Wavefront Manipulation

This section focuses on the application of the proposed ultra-thin single-layer MS for comprehensive and multifunctional wavefront manipulation across the entire space, utilizing the principles of geometric phase. The geometric phase, also referred to as the Pancharatnam-Berry (PB) phase, serves as a powerful tool for controlling the wavefront properties of CP waves. By incorporating the geometric phase concept, the MS is capable of inducing equal and opposite phase shifts on the two orthogonal CP states, resulting in a dispersion-less response that is solely determined by the orientation angle of the resonator structure. With the geometric phase MS, a complete range of 2π phase shift can be achieved by simply rotating the resonator structure to a specific orientation angle, while maintaining a constant amplitude for the orthogonal CP wave.

By introducing a local orientation angle α in the designed unit-cell structure of MS, the CP wave can undergo conversion to its orthogonal component, accompanied by a sudden phase shift of $\pm 2\alpha$ during reflection or transmission. Consequently, the proposed MS offers the capability to achieve various CP wavefront manipulations by arranging unit-cells with different α. In order to comprehensively manipulate the CP wavefront across the entire space using the proposed MS, it is necessary to investigate whether rotating the α of the unit-cell structure can yield a complete 2π phase shift, while simultaneously maintaining high amplitudes of the orthogonal CP wave for both reflection and transmission modes. Fig. 4(a) and (c) present the simulated amplitudes of the reflected and transmitted orthogonal CP waves for the proposed structure with eight different orientation angles (α), under normal incident LCP and RCP waves propagating along the negative z-axis direction. The simulated amplitudes of the reflected and transmitted orthogonal CP waves for unit-cell structures with varying α, in steps of 22.5°, are nearly identical and consistently above 0.3, which aligns with the experimental findings (refer to Fig. 2(a) and (c)). The corresponding phases of the reflected and transmitted orthogonal CP waves for the designed MS structure with different α, also in steps of 22.5°, are depicted in Fig. 4(b) and (d). It is evident that the phase

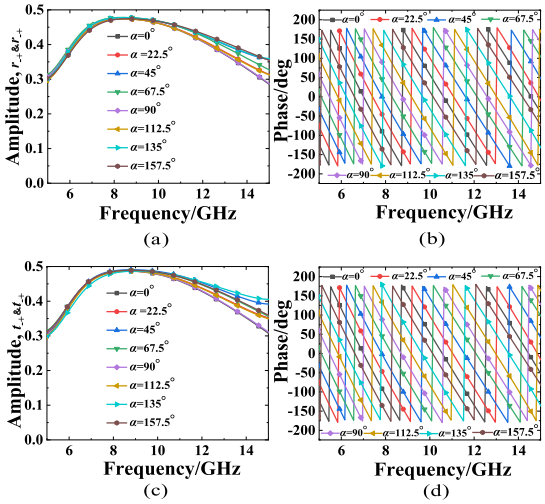

Fig. 4. Simulated (a), (c) amplitude and (b), (d) phase of the (a), (b) reflected and (c), (d) transmitted orthogonal CP wave for the MS unit-cell with different rotation angles α under normal incident LCP/RCP wave.

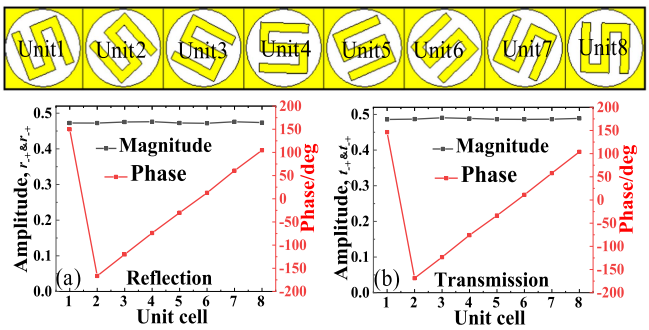

Fig. 5. Schematic diagram of the MS supercell with eight unit-cell different α and the corresponding amplitude and phase of the (a) reflected and (b) transmitted orthogonal CP wave under normal incident LCP wave at 9 GHz.

shift between adjacent α values is approximately 45° over the broadband frequency range of 5 GHz to 15 GHz. Additionally, the phase variation of the reflected and transmitted orthogonal CP waves exhibits a nearly linear relationship with the change in α within the aforementioned broadband range. Thus, by manipulating α, the full range of 2π phase-shift can be achieved. The proposed SSR structure enables broadband CP conversion and 2π phase control for both reflection and transmission. Numerical simulations serve as evidence for the effectiveness of the proposed single-layer MS in achieving full-space wavefront manipulation, anomalous reflection and refraction, full-space vortex beam generation, and planar focusing effects.

1) Anomalous Reflection and Refraction: To investigate the anomalous reflection and refraction effect of the incident CP waves, Fig. 5 showcases a MS supercell consisting of eight unit-cells with different α and presents the amplitudes and phases of the reflected and transmitted orthogonal CP waves at a frequency of 9 GHz. By employing the MS supercell, a linear gradient phase spanning from 0 to 2π is achieved for both reflection and transmission. The amplitudes of the orthogonal CP waves for reflection and transmission remain consistently

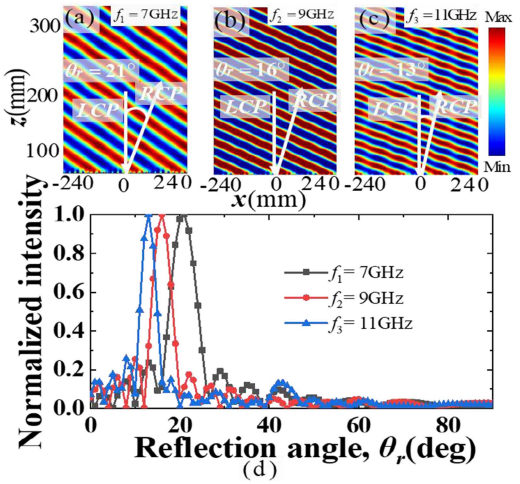

Fig. 6. Simulated space electric field distributions in x-z plane of the reflected RCP wave under the normal incident LCP waves propagating along the z-axis direction at (a) 7 GHz, (b) 9 GHz and (c) 11 GHz, (d) the corresponding normalized intensity of the reflected wave.

high, approximately 0.47, as we progress from Unit1 to Unit8. Moreover, the 2π phase coverage is achieved at 9 GHz. These findings highlight the capability of the proposed MS supercell, based on the geometric phase principle, to facilitate abnormal reflection and refraction.

In the context of a free spece environment and normal incident CP wave ($n_i = 1$ and $\theta_i = 0°$), the deflection angles of the reflected and transmitted waves can be derived using the generalized Snell's law [39]:

$$\theta_r = \sin^{-1}\left(\frac{\lambda_o}{pN}\right) \tag{1}$$

$$\theta_t = \sin^{-1}\left(\frac{\lambda_o}{pN}\right) \tag{2}$$

In the equations provided, θ_r, θ_t, and θ_i represent the angles of reflection, refraction, and incidence of the CP wave, respectively. The refractive index of the free space environment is denoted by n_i, while λ_0 corresponds to the operating wavelength. Additionally, p represents the lattice length of a unit-cell, and N denotes the number of unit-cells within the operating wavelength range.

For the specific design of anomalous reflection and refraction in the MS, N is set to 8, p is set to 15mm, and the typical operating frequencies are $f_1 = 7$GHz, $f_2 = 9$GHz, and $f_3 = 11$GHz. The theoretical calculations indicate that for normal incident LCP waves, the corresponding values of θ_r and θ_t for the proposed single-layer MS are approximately 20.92°, 16.12°, and 13.13° at 7 GHz, 9 GHz, and 11 GHz, respectively.

To further illustrate the anomalous reflection and refraction capabilities of the proposed MS for normal incident CP waves, we present simulated electric field distributions and normalized intensity profiles of the reflected and transmitted RCP waves. The simulations depict a scenario where a normal incident left LCP wave propagates along the z-axis direction at frequencies of 7 GHz, 9 GHz, and 11 GHz, as shown in Figs. 6 and 7. It is observed that both the reflected and transmitted

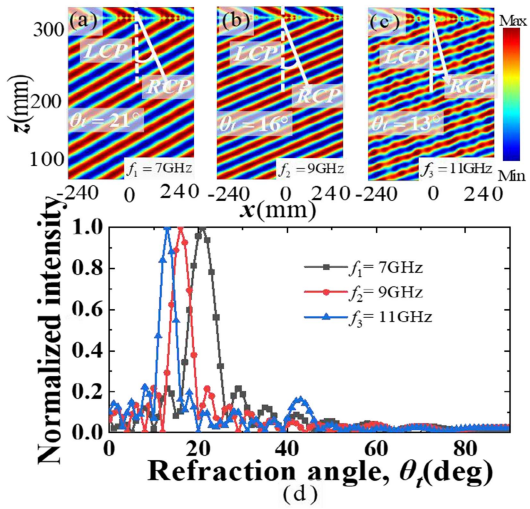

Fig. 7. Simulated electric field distributions in x-z plane of the transmitted RCP wave under the normal incident LCP waves propagating along the z-axis direction at (a) 7 GHz, (b) 9 GHz and (c) 11 GHz, (d) the corresponding normalized intensity of the transmitted wave.

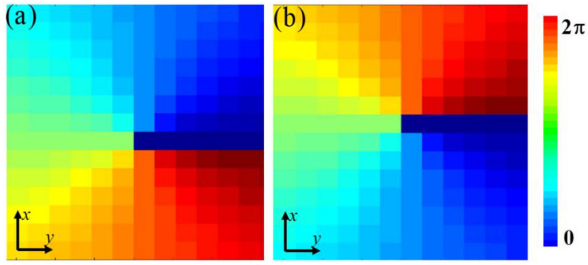

Fig. 8. Phase distributions of the proposed (a) reflection and (b) transmission MS for the generated vortex beam with topological charge of $l = +1$.

waves exhibit oblique directions relative to the z-axis direction, indicating a successful conversion of the incident LCP wave into its orthogonal CP component and deflection in anomalous directions. Moreover, the deflection angles decrease as the operating frequency increases, for both reflection and transmission. Specifically, the deflection angles of the reflected and transmitted waves are found to be 21°, 16°, and 13° at 7 GHz, 9 GHz, and 11 GHz, respectively, which closely align with the theoretical predictions of 20.92°, 16.12°, and 13.13°.

The normalized intensity profiles of the reflected and transmitted waves, depicted in Figs. 6(d) and 7(d), respectively, indicating that they approach unity at the corresponding deflection angles of 21°, 16°, and 13° for the frequencies 7 GHz, 9 GHz, and 11 GHz. These findings are consistent with the theoretical predictions, confirming the effectiveness of the proposed single-layer MS as a beam deflector for CP waves in both reflection and transmission modes. The achieved deflection angles of 21°, 16°, and 13° at 7 GHz, 9 GHz, and 11 GHz, respectively, under normal incident LCP wave align with the expected behavior of the system.

2) Vortex Beam Generation: The generation of vortex beams, which carry OAM, holds significance in wireless communication and can be achieved using MS when illuminated with CP waves [20], [28], [44], [45]. A vortex beam with OAM possesses a phase distribution of $e^{il\varphi}$ at the transverse plane, where l represents the topological charge and φ denotes the azimuthal angle. The OAM is associated with the spiral phase front of the spatial distribution, forming the orbital component of the vortex beam. This section focuses on numerically demonstrating the generation of vortex beams carrying OAM using the designed single-layer MS, both in reflection and transmission. To achieve the desired vortex beam with a spiral phase profile, the unit-cells within the MS need to be arranged in a spiral shape. The phase distribution of each unit-cell position (x, y) should be carefully designed to correspond with the azimuthal angle φ around the central point (0,0), ensuring the desired spiral phase profile of the vortex beam is obtained [46]:

$$\varphi(x, y) = l \cdot \arctan\left(\frac{y}{x}\right) \tag{3}$$

the symbol $\varphi(x, y)$ represents the necessary phase distribution for a specific location, while the variable l indicates the desired OAM topological charge, which determines the specific vortex beam of the l-th order by modifying the phase arrangements within the MS. The value of l can be any integer (±1, ±2, ±3, etc.), and the corresponding azimuthal phase variation can span a phase range of $l \times 2\pi$ by utilizing the specially designed MS.

To achieve vortex beams with various topological charges, different phase arrangements can be utilized. However, in this particular study, our focus is on generating full-space vortex beams using a simplified design approach for the proposed single-layer MS. For this purpose, we divide the MS into eight triangular regions and concentrate on generating a vortex beam with a topological charge of $l = +1$. Fig. 8 illustrates the phase distributions of the proposed MS for both reflection and transmission modes, enabling the generation of vortex beams carrying OAM with a topological charge of $l = +1$. Within the MS, the adjacent regions maintain a phase gradient of $\pi/6$, resulting in phase values ranging from 0 to 2π for a complete revolution around the beam axis in both reflection and transmission modes. To implement the generation of vortex beams in both reflection and transmission modes, the proposed MS consists of a total of 14×12 unit cells, covering an area of 210×180 mm^2.

The reflection and transmission of CP vortex beams produced by the proposed single-layer MS were simulated using the FIT. In the simulation, open boundaries are employed in both the x and y directions to model the MS array accurately. To mitigate any truncation effects resulting from the edges of the MS, LCP Gaussian beams are illuminated on the xoy plane of the designed MS, propagating along the negative z-direction [20].

Figs. 9 and 10 depict the near-field phase and intensity distributions of reflected and transmitted vortex beams carrying OAM with a topological charge of $l = +1$, respectively, at frequencies of 7 GHz, 9 GHz, and 11 GHz. Across these frequencies, both the reflected and transmitted vortex beams exhibit characteristic near-field spiral phase distributions indicative of OAM with a topological charge of $l = +1$. Additionally, these distributions feature pairs of spiral arms, with opposite rotational directions

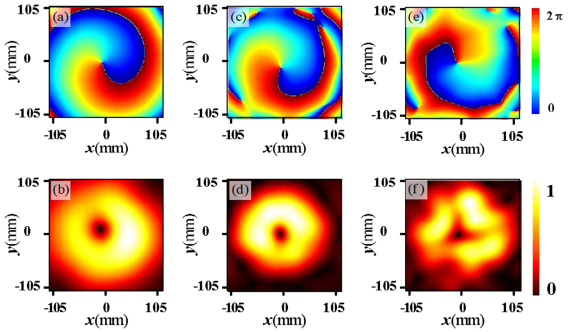

Fig. 9. Simulated distributions of (a), (c), (e) phases and (b), (d), (f) intensity of the reflected vertex beams with topological charge of $l = +1$ at (a)–(b) 7GHz, (c)–(d) 9GHz and (e)–(f) 11G Hz for the proposed MS for the normal incident LCP wave.

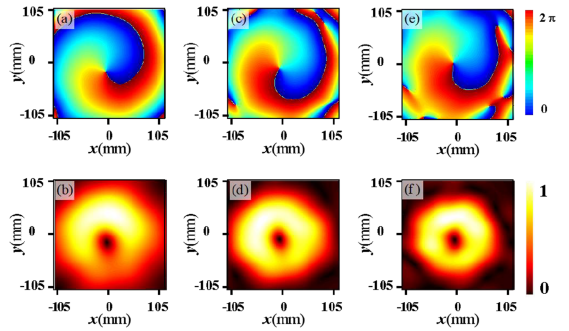

Fig. 10. Simulated distributions of (a), (c), (e) phases and (b), (d), (f) intensity of the transmitted vertex beams with topological charge of $l = +1$ at (a)–(b) 7GHz, (c)–(d) 9GHz and (e)–(f) 11G Hz for the proposed MS for the normal incident LCP wave.

observed in both reflection (as shown in Fig. 9(a), (c), and (e) and transmission modes (as shown in Fig. 10(a), (c), and (e). These findings suggest that the generation of reflected and transmitted vortex beams occurs over a wide frequency range spanning from 7 GHz to 11 GHz. Furthermore, the central region of the vortex beam with a topological charge of $l = +1$ displays a near-zero intensity area attributed to the presence of a near-field phase singularity, as illustrated in Figs. 9(b), (d), and (f) and 10(b), (d), and (f). It is worth noting that the proposed single-layer MS has the potential to generate a range of vortex beams with higher-order topological charges (e.g., $l = \pm 2, \pm 3, \pm 4$, etc.) for both reflection and transmission across a broadband frequency range (not shown).

To assess the efficacy of the designed MS in generating reflection and transmission vortex beams, we employed the discrete Fourier transform (DFT) algorithm to calculate the OAM mode purities of vortex beams with a topological charge of $l = +1$ at three distinct frequencies. By applying the spiral harmonics $e^{il\phi}$ to analyze the electric field projection, Fourier spectral analysis allows us to evaluate the primary and secondary mode powers of the generated vortex beams with varying topological charges [20], [27]. Fig. 11 presents the OAM mode purities of the reflected and transmitted vortex beams with a topological charge of $l = +1$ at frequencies of 7 GHz, 9 GHz, and 11 GHz for normally incident LCP Gaussian waves. The main OAM mode purities for the reflected vortex beam with a topological charge of $l = +1$ reach values of 69.4%, 62.9%, and 55.2%, while the corresponding transmission purities are 64.9%, 60.1%, and 59.7% at the aforementioned frequencies. These findings indicate that the desired OAM modes dominate at all three frequencies, thereby demonstrating the high quality of the generated vortex beams for both reflection and transmission modes. Furthermore, the purities of other OAM modes remain below 15% at these frequencies, suggesting the presence of minor phase noise. Hence, it is evident that the proposed MS can effectively generate broadband vortex beams for both reflection and transmission modes.

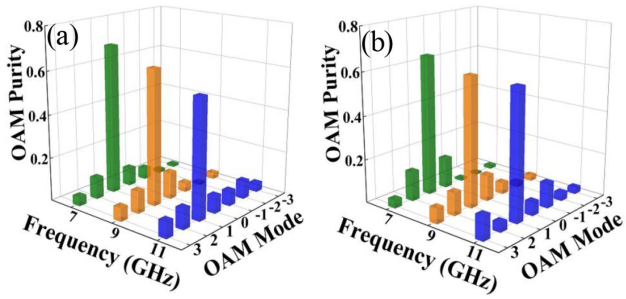

Fig. 11. Calculated OAM mode purity of the (a) reflected and (b) transmitted vortex beam of the proposed MS with topological charge of $l = +1$ at three typical frequencies ($f = 7$GHz, 9GHz, 11GHz).

3) Planar Focusing Effect: The planar focusing effect achieved through meta-lenses based on MSs is widely regarded as a highly promising EM device, offering distinct advantages in terms of functionality and performance compared to conventional lenses [29], [35], [39], [47]. Leveraging the planar focusing effect simplifies numerous focusing components, facilitating the integration of EM devices into modern systems. Specifically, the utilization of specialized MSs with discontinuous phase gradients enables the realization of diverse meta-lens designs [47].

In this section, we provide a comprehensive demonstration of the planar focusing effect in both reflection and transmission modes, utilizing the designed MS structure. To achieve complete spatial focusing for the incident CP wave, precise calculations are performed to determine the specific orientation rotation angle of each unit-cell on the xoy plane. This calculation compensates for the necessary phase delay required for effective focusing. The phase distribution of the meta-lens in the xoy plane can be generally determined using the following equation [47], [48], [49], [50]:

$$\varphi(x, y) = \frac{2\pi}{\lambda}\left(\sqrt{x^2 + y^2 + F^2} - F\right) \tag{4}$$

where $\varphi(x, y)$ represents the phase compensation at special point (x,y) of the xoy plane, F is the focal length and λ is the operation wavelength.

Fig. 12 provides a schematic representation of the specially designed MS structure and depicts the corresponding phase distributions in the xoy plane for both reflection and transmission

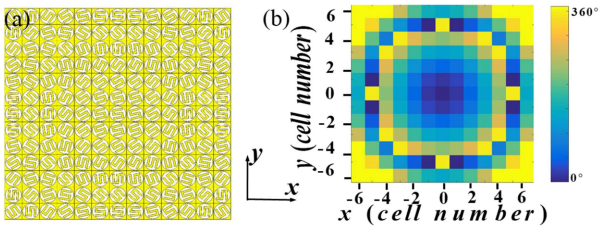

Fig. 12. (a) Schematic diagrams of the 2D array of the designed MSs at 7GHz, (b) the corresponding phase distribution in *xoy* plane.

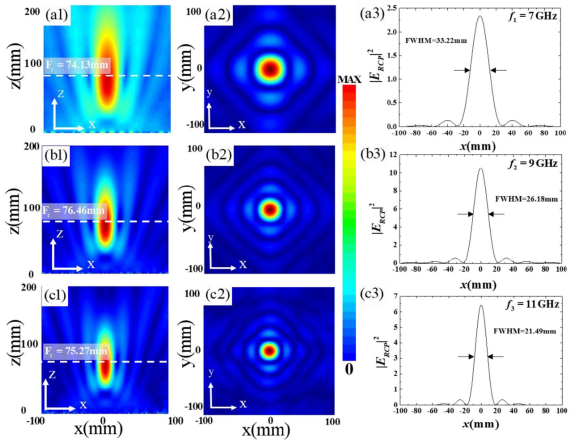

Fig. 13. (a) The simulated 2D electric field ($|E|$) distributions in the (a1)–(c1) *x*-*z* plane and (a2)–(c2) *x*-*y* plane of (a) the reflected CP wave at (a1)–(a2) 7 GHz, (b1)–(b2) 9 GHz and (c1)–(c2) 11 GHz, (a3)–(c3) the corresponding electrical field intensity ($|E_{RCP}|^2$) profile on focal plane at the above three frequencies.

modes. The proposed single-layer meta-lens, based on the MS structure, exhibits the capability to achieve the focusing effect for both reflection and transmission. As depicted in Fig. 12(a), the meta-lens is constructed by arranging 13 × 13 unit-cell structures. The phase distribution across the xoy plane of the MS enables complete coverage of a 2π phase in both the x- and y-axis directions, as illustrated in Fig. 12(b). To demonstrate the full-space focusing effect of the MS-based meta-lens, a pre-determined theoretical focal length of 80 mm and operating frequencies of 7 GHz, 9 GHz, and 11 GHz were selected. The simulation was conducted using open boundary conditions, with an incident LCP wave propagating along the -z direction serving as the excitation source.

Figs. 13 and 14 showcase the simulated electric field distributions ($|E|$) in the x-z and x-y planes, as well as the corresponding intensity profiles ($|E_{RCP}|^2$) on the focal plane of the reflected and transmitted orthogonal CP waves across frequencies of 7 GHz, 9 GHz, and 11 GHz. In Fig. 13(a1)–(c1), the electric field of the reflected orthogonal CP wave exhibits a concentrated pattern around specific positions, namely z = 74.13 mm, 76.66 mm, and 75.27 mm, within the x-z plane when the incident LCP plane wave propagates along the z-axis direction. Notably, these positions give rise to distinct bright spots at the respective frequencies. The practical focal length F_r for the reflected orthogonal CP wave is thereby estimated to be approximately 74.13

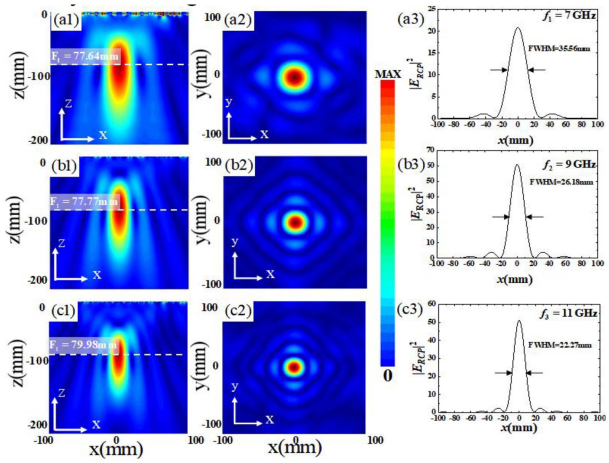

Fig. 14. (a) The simulated 2D electric field ($|E|$) distributions in the (a1)–(c1) *x*-*z* plane and (a2)–(c2) *x*-*y* plane of (a) the transmitted CP wave at (a1)–(a2) 7 GHz, (b1)–(b2) 9 GHz and (c1)–(c2) 11 GHz, (a3)–(c3) the corresponding electrical electrical intensity ($|E_{RCP}|^2$) profile on focal plane at the above three frequencies.

mm, 76.66 mm, and 75.27 mm at these frequencies, respectively, which aligns closely with the theoretical focal length of 80 mm.

Furthermore, as depicted in Fig. 13(a2)–(c2), a distinct bright spot is observed at the central position of the focal plane, indicating effective convergence of EM energy for the reflected orthogonal CP wave across a wide frequency range. The full-width half maximums (FWHM) of the electric field intensity ($|E_{LCP}|^2$) along the x-axis direction for the reflected orthogonal CP wave, as illustrated in Fig. 13(a3)–(c3), measure approximately 33.22 mm, 26.18 mm, and 21.49 mm at 7 GHz, 9 GHz, and 11 GHz, respectively. These findings demonstrate a notable subwavelength focusing effect in reflection achieved by the designed meta-lens, covering a broad frequency spectrum. It is worth noting that the FWHM value depends heavily on the aperture size of the MS-based meta-lens and can be further reduced by increasing the total number of unit-cells.

We now proceed to assess the focusing performance of our design in the transmission mode, which is illuminated by an LCP plane wave. Similar to the reflection mode, the simulated 2D electric field distributions on the x-z plane and x-y plane at the operating frequency vividly illustrate the exceptional focusing effect in the transmission mode. As shown in Fig. 14(a1)–(c1), the focal length F_t of the transmitted orthogonal CP wave measures approximately 77.64 mm, 77.77 mm, and 79.98 mm at 7 GHz, 9 GHz, and 11 GHz, respectively, closely matching the theoretical value of 80 mm. In Fig. 14(a2)–(c2), a distinct bright spot at the central position of the focal plane is clearly observed at these frequencies, indicating efficient convergence of EM energy to a focal point after transmission through the designed meta-lens across a wide frequency range.

Moreover, Fig. 14(a3)–(c3) demonstrates that the calculated full-width half maximum (FWHM) of the electric field intensity ($|E_{LCP}|^2$) along the x-axis direction for the transmitted orthogonal CP wave is approximately 35.56 mm, 26.18 mm, and 22.27 mm at 7 GHz, 9 GHz, and 11 GHz, respectively, signifying

TABLE I
COMPARISON FOR FULL-SPACE MSS REALIZED IN LITERATURES

References	Structure configuration	Polairzation	Operation efficiency	Fractional bandwidth	Application demonstrated
[35]	Four-layers	LP	85%–91%	9.5%	Bend, focusing
[36]	Five-layers	LP	90%	9.6%	Deflection, diffuse RCS, and OAM
[37]	Single-layer	CP	20%	112%	Deflection and OAM
[38]	Three-layer	LP	60%-80%	13.3%	
[39]	Two-layer	CP	85%-90%	16.6%	Deflection, focusing and OAM
[40]	Five-layers	LP	90%	41.1%	OAM
This work	Single-layer	CP	23%	87.1%	Deflection, focusing and OAM

a pronounced focusing effect in transmission achieved by our meta-lens over a broadband frequency range. Additionally, the maximum intensity of the transmitted CP wave is approximately 22, 62, and 53 times higher than that of the incident wave at these frequencies, highlighting the remarkable focusing effect during transmission enabled by the designed meta-lens.

It is noteworthy that the designed MS has achieved successful realization of a broadband CP conversion and full-space wavefront manipulation applications. This accomplishment demonstrates a high level of comparability with previous studies in the field [35], [36], [37], [38], [39], [40]. The proposed MS design scheme has been compared to recently reported designs based on various performance parameters such as structure configuration, polarization, operation efficiency, fractional bandwidth and applocation demonstrated. According to the comparison presented in Table I, a clear improvement can be observed, indicating that the proposed MS design outperforms the previously reported designs in one or more of the mentioned performance parameters.

IV. CONCLUSION

In conclusion, we demonstrated a novel design of an ultra-thin MS that consists of a copper SSR structure enclosed by a copper circular cover on a dielectric substrate. This design achieves broad CP conversion with equal parts reflection and transmission, as well as versatile wavefront manipulation capabilities in the microwave range. Simulation results demonstrate that the amplitudes of the orthogonal CP wave in both reflection and transmission modes exceed 0.35 across a frequency range of 6.2 GHz to 15 GHz, with a fractional bandwidth of 83%, which aligns well with experimental measurements. Leveraging the geometric phase principle, the MS achieves complete 2π phase coverage for both modes over the entire broadband frequency range. Three MS devices are designed and numerically demonstrated to realize anomalous reflection and refraction, vortex beam generation, and planar focusing functionalities in both transmission and reflection modes within a wide frequency range, thereby confirming the concept of comprehensive and multifunctional wavefront manipulation. Moreover, by scaling the unit-cell structure, the proposed single-layer MS can effectively operate in the terahertz, infrared, and even optical regions. With its exceptional features of broad CP conversion and versatile wavefront manipulation, we anticipate that our proposed MS will greatly impact the design of electromagnetic wave modulating devices.

REFERENCES

[1] N. Yu and F. Capasso, "Flat optics with designer metasurfaces," *Nature Mater.*, vol. 13, pp. 139–150, Jan. 2014.

[2] H. T. Chen, A. J. Taylor, and N. Yu, "A review of metasurfaces: Physics and applications," *Rep. Prog. Phys.*, vol. 79, no. 7, Jul. 2016, Art. no. 076401.

[3] Y. Cheng and J. Zhao, "Simple design of a six-band terahertz perfect metasurface absorber based on a single resonator structure," *Physica Scripta*, vol. 97, Sep. 2022, Art. no. 095508.

[4] Y. Z. Cheng, Y. J. Qian, H. Luo, F. Chen, and Z. Z. Cheng, "Terahertz narrowband perfect metasurface absorber based on micro-ring-shaped GaAs array for enhanced refractive index sensing," *Physica E: Low-Dimensional Syst. Nanostructures*, vol. 146, Jan. 2023, Art. no. 115527.

[5] I. P. Radko et al., "Plasmonic metasurfaces for waveguiding and field enhancement," *Laser Photon. Rev.*, vol. 3, no. 6, pp. 575–590, Oct. 2009.

[6] Z.-L. Deng, Y. Cao, X. Li, and G. P. Wang, "Multifunctional metasurface: From extraordinary optical transmission to extraordinary optical diffraction in a single structure," *Photon. Res.*, vol. 6, no. 5, pp. 443–450, 2018.

[7] Q. Zheng, C. Guo, and J. Ding, "Wideband metasurface-based reflective polarization converter for linear-to-linear and linear-to-circular polarization conversion," *IEEE Antennas Wireless Propag. Lett.*, vol. 17, no. 8, pp. 1459–1463, Aug. 2018.

[8] Y. Z. Cheng, X. Z. Zhu, J. Li, F. Chen, H. Luo, and L. Wu, "Terahertz broadband tunable reflective cross-polarization convertor based on complementary cross-shaped graphene metasurface," *Physica E: Low-Dimensional Syst. Nanostructures*, vol. 134, Oct. 2021, Art. no. 114893.

[9] P. Genevet and F. Capasso, "Holographic optical metasurfaces: A review of current progress," *Rep. Prog. Phys.*, vol. 78, no. 2, Jan. 2015, Art. no. 024401.

[10] H. Gao, X. Fan, W. Xiong, and M. Hong, "Recent advances in optical dynamic meta-holography," *Opto-Electron. Adv.*, vol. 4, no. 4, Nov. 2021, Art. no. 210030.

[11] S. Liu et al., "Anisotropic coding metamaterials and their powerful manipulation of differently polarized terahertz waves," *Light: Sci. Appl.*, vol. 5, Jan. 2016, Art. no. e16076.

[12] X. Chen et al., "Dual-polarity plasmonic metalens for visible light," *Nature Commun.*, vol. 3, no. 1, Nov. 2012, Art. no. 1198.

[13] S. Wang et al., "A broadband achromatic metalens in the visible," *Nature Nanotechnol.*, vol. 13, pp. 227–232, Jan. 2018.

[14] G.-Y. Deng et al., "Ultrabroadband RCS reduction design by exploiting characteristic complementary polarization conversion metasurfaces," *IEEE Trans. Antennas Propag.*, vol. 70, no. 4, pp. 2904–2914, Apr. 2022.

[15] E. Y. Zhou, Y. Z. Cheng, F. Chen, and H. Luo, "Wideband and high-gain patch antenna with reflective focusing metasurface," *AEU-Int. J. Electron. Commun.*, vol. 134, May 2021, Art. no. 153709.

[16] M. Khanjarian, M. Soleimani, V. Nayyeri, M. E. Badawe, S.-F. Babazadeh, and O. M. Ramahi, "A circularly polarized, high aperture efficiency metasurface antenna," *Microw. Opt. Technol. Lett.*, vol. 63, no. 12, pp. 3027–3034, Dec. 2021.

[17] J. X. Wang, J. C. Zhao, Y. Z. Cheng, H. Luo, and F. Chen, "Dual-band high-gain microstrip antenna with a reflective focusing metasurface for linear and circular polarizations," *AEU-Int. J. Electron. Commun.*, vol. 157, no. 2, Sep. 2022, Art. no. 154413.

[18] B. He, J. P. Fan, Y. Z. Cheng, F. Chen, H. Luo, and R. Z. Gong, "Thermally tunable terahertz vortex beam generator based on an InSb metasurface," *J. Opt. Soc. Amer. B*, vol. 38, no. 5, pp. 1518–1524, Mar. 2021.

[19] J. H. Lin, C. Chen, J. Ding, S. Wang, and W. D. Chen, "Dual-frequency multiple compact vortex beams generation based on single-layer Bi-spectral metasurface," *Appl. Phys. Lett.*, vol. 119, Aug. 2021, Art. no. 081905.

[20] J. Q. Liu, Y. Z. Cheng, F. Chen, H. Luo, and X. C. Li, "High-efficiency reflective metasurfaces for terahertz vortex wave generation based on completely independent geometric phase modulations at three frequencies," *J. Opt. Soc. Amer. B*, vol. 39, no. 7, pp. 1752–1761, May 2022.

[21] M. Khorasaninejad, W. T. Chen, R. C. Devlin, J. Oh, A. Y. Zhu, and F. Capasso, "Metalenses at visible wavelengths: Diffraction-limited focusing and subwavelength resolution imaging," *Science*, vol. 352, no. 6290, pp. 1190–1194, Jun. 2016.

[22] H.-X. Xu et al., "Deterministic approach to achieve full-polarization cloak," *Research*, vol. 2021, Mar. 2021, Art. no. 6382172.

[23] Q. Ma et al., "Directly wireless communication of human minds via non-invasive brain-computer metasurface platform," *eLight*, vol. 2, no. 1, pp. 1–11, Jun. 2022.

[24] J. Zhao, N. Li, and Y. Cheng, "All-dielectric InSb metasurface for broadband and high-efficient thermal tunable terahertz reflective linear-polarization conversion," *Opt. Commun.*, vol. 536, Mar. 2023, Art. no. 129372.
[25] H. Liu, H. Xue, Y. Liu, Q. Feng, and L. Li, "Generation of high-order Bessel orbital angular momentum vortex beam using a single-layer reflective metasurface," *IEEE Access*, vol. 8, pp. 126504–126510, 2020.
[26] H. Lu et al., "Frequency-controlled focusing using achromatic metasurface," *Adv. Opt. Mater.*, vol. 9, no. 1, Nov. 2020, Art. no. 2001311.
[27] C. Wang et al., "Heterogeneous amplitude-phase metasurface for distinct wavefront manipulation," *Adv. Photon. Res.*, vol. 2, no. 10, Jun. 2021, Art. no. 2100102.
[28] M. C. Wang, Y. Z. Cheng, and L. Wu, "Ultra-broadband high-efficiency circular polarization conversion and terahertz wavefront manipulation based on an all-metallic reflective metasurface," *Appl. Opt.*, vol. 61, no. 16, pp. 4833–4842, Jun. 2022.
[29] X. Z. Zhu, Y. Z. Cheng, J. P. Fan, F. Chen, H. Luo, and L. Wu, "Switchable efficiency terahertz anomalous refraction and focusing based on graphene metasurface," *Diamond Related Mater.*, vol. 121, Jan. 2022, Art. no. 108743.
[30] L. L. Li, H. T. Zhao, C. Liu, L. Li, and T. J. Cui, "Intelligent metasurfaces: Control, communication and computing," *eLight*, vol. 2, no. 7, May 2022, Art. no. 7.
[31] J. X. Li et al., "Hybrid dispersion engineering based on chiral metamirror," *Laser Photon. Rev.*, vol. 17, no. 3, Jan. 2023, Art. no. 2200777.
[32] Y. Y. Yuan, Q. Wu, S. N. Burokur, and K. Zhang, "Chirality-assisted phase metasurface for circular polarization preservation and independent hologram imaging in microwave region," *IEEE Trans. Microw. Theory Techn.*, early access, Mar. 21, 2023, doi: 10.1109/TMTT.2023.3256527.
[33] Y. Tamayama, K. Yasui, T. Nakanishi, and M. Kitano, "A linear-to-circular polarization converter with half transmission and half reflection using a single-layered metamaterial," *Appl. Phys. Lett.*, vol. 105, Jul. 2014, Art. no. 021110.
[34] X. M. Ding et al., "Ultrathin Pancharatnam–Berry metasurface with maximal cross-polarization efficiency," *Adv. Mater.*, vol. 27, no. 7, pp. 1195–1200, 2015.
[35] T. Cai et al., "High-efficiency and full-space manipulation of electromagnetic wave fronts with metasurfaces," *Phys. Rev. Appl.*, vol. 8, 2017, Art. no. 034033.
[36] L. Zhang et al., "Transmission-reflection-integrated multifunctional coding metasurface for full-space controls of electromagnetic waves," *Adv. Funct. Mater.*, vol. 28, no. 33, Jun. 2018, Art. no. 1802205.
[37] M. R. Akram, G. W. Ding, K. Chen, Y. J. Feng, and W. R. Zhu, "Ultrathin single layer metasurfaces with ultra-wideband operation for both transmission and reflection," *Adv. Mater.*, vol. 32, no. 12, Feb. 2020, Art. no. 1907308.
[38] L. Bao, X. J. Fu, R. Y. Wu, Q. Ma, and T. J. Cui, "Full-space manipulations of electromagnetic wavefronts at two frequencies by encoding both amplitude and phase of metasurface," *Adv. Mater. Technol.*, vol. 6, no. 4, Feb. 2021, Art. no. 2001032.
[39] J. P. Fan, Y. Z. Cheng, and B. He, "High-efficiency ultrathin terahertz geometric metasurface for full-space wavefront manipulation at two frequencies," *J. Phys. D: Appl. Phys.*, vol. 54, no. 11, Mar. 2021, Art. no. 115101.
[40] Z. T. Zhang et al., "Multifunctional full-space metasurface controlled by frequency, polarization and incidence angle," *Opt. Exp.*, vol. 29, no. 5, pp. 7544–7557, Mar. 2021.
[41] T. Lu et al., "Single-layer ultra-wideband multifunctional transmissive metasurface," *IEEE Trans. Antennas Propag.*, vol. 70, no. 8, pp. 6850–6857, Aug. 2022.
[42] Y. H. Tan et al., "Free-standing single-layer metasurface for efficient and broadband tailoring of terahertz wavefront," *Adv. Opt. Mater.*, vol. 10, no. 16, May 2022, Art. no. 2200565.
[43] J. Y. Wang et al., "Transmission–reflection-integrated quadratic phase metasurface for multifunctional electromagnetic manipulation in full space," *Adv. Opt. Mater.*, vol. 10, 2022, Art. no. 2102111.
[44] N. Yu et al., "Ultra-thin plasmonic optical vortex plate based on phase discontinuities," *Appl. Phys. Lett.*, vol. 100, no. 1, 2012, Art. no. 013103.
[45] Z. Xu, C. Ni, Y. Cheng, L. Dong, and L. Wu, "Photo-excited metasurface for tunable terahertz reflective circular polarization conversion and anomalous beam deflection at two frequencies independently," *Nanomaterials*, vol. 13, no. 12, 2023, Art. no. 1846.
[46] J. Li, Y. Z. Cheng, J. P. Fan, F. Chen, H. Luo, and X. C. Li, "High-efficiency terahertz full-space metasurface for the transmission linear and reflection circular polarization wavefront manipulation," *Phys. Lett. A*, vol. 428, 2022, Art. no. 127932.
[47] X. Zhu, Y. Cheng, F. Chen, H. Luo, and L. Wu, "Efficiency adjustable terahertz circular polarization anomalous refraction and planar focusing based on a bi-layered complementary Z-shaped graphene metasurface," *J. Opt. Soc. Amer. B*, vol. 39, no. 3, pp. 705–712, Mar. 2022.
[48] D. R. Yang, Y. Z. Cheng, F. Chen, H. Luo, and L. Wu, "Efficiency tunable broadband terahertz graphene metasurface for circular polarization anomalous reflection and plane focusing effect," *Diamond Related Mater.*, vol. 131, 2023, Art. no. 109605.
[49] D. R. Yang, Y. Z. Cheng, H. Luo, F. Chen, and L. Wu, "Ultrathin and ultra-broadband terahertz single-layer metasurface based on double-arrow-shaped resonator structure for full-space wavefront manipulation," *Adv. Theory Simulations*, vol. 5, 2023, Art. no. 2300162.
[50] C. Ni, L. Dong, Z. Xu, M. Wang, L. Wu, and Y. Cheng, "Broadband and high-efficiency thermal switchable InSb metasurface for terahertz wave anomalous reflection and focusing effect," *Mater. Today Commun.*, vol. 35, 2023, Art. no. 106305.